Enhanced surface structuring by ultrafast XUV/NIR dual action

2011 New J. Phys. 13 053049

(http://iopscience.iop.org/1367-2630/13/5/053049)

New Journal of Physics
The open-access journal for physics

Enhanced surface structuring by ultrafast XUV/NIR dual action

Krzysztof Jakubczak[1,3,4], Tomas Mocek[1], Jaromir Chalupsky[1], Gae Hwang Lee[2], Tae Keun Kim[2], Seung Beom Park[2], Chang Hee Nam[2], Vera Hajkova[1], Martina Toufarova[1], Libor Juha[1] and Bedrich Rus[1]

[1] Institute of Physics AS CR, Na Slovance 2, 182 21 Prague, Czech Republic
[2] Department of Physics and Coherent X-ray Research Center, Korea Advanced Institute of Science and Technology (KAIST), 373-1, Kusong-dong, Yusong-gu, Daejon 305-701, Korea
E-mail: kkjakubczak@gmail.com

New Journal of Physics **13** (2011) 053049 (12pp)
Received 13 October 2010
Published 25 May 2011
Online at http://www.njp.org/
doi:10.1088/1367-2630/13/5/053049

Abstract. Materials processing utilizing ultrashort near-infrared (NIR) laser pulses with duration in the range of tens to hundreds of femtoseconds (1 fs = 10^{-15} s) has attracted a great deal of interest in the scientific and industrial world recently. Unfortunately, a number of materials that often exhibit great technological and scientific importance are transparent in NIR, making it very difficult to process them by laser radiation in this spectral range. Here, we present a new method for the efficient structuring of the surface of materials by applying femtosecond NIR laser pulses simultaneously with a weak extreme ultraviolet (XUV) beam, which leads to very strong radiation–matter interaction, bringing a dramatic increase in the surface processing speed. A laser system providing 5 mJ, 820 nm, 32 fs, 10 Hz pulses was used to generate high-order harmonics with the strongest spectral line at 21 nm and with a conversion efficiency of ∼5%. The two beams were focused on the samples by using an off-axis paraboloidal multilayer mirror. As an example, we present the results of the surface nanostructuring of thin films of amorphous carbon and poly(methyl methacrylate) deposited on bulk substrates. We discuss the physical mechanisms that lead to the laser-induced periodic surface structures when our method is used.

[3] Author to whom any correspondence should be addressed.
[4] Present address: Croma Polska sp. z o.o., 31 Ryzowa Str., 02–495 Warsaw, Poland.

Contents

1. Introduction

With the advent of table-top, high-repetition-rate, femtosecond laser systems, there has been a great deal of interest in the field of materials machining using ultrashort laser pulses. The applicability of femtosecond laser pulses in material science has been demonstrated by numerous experiments, including experiments on the processing of semiconductors [1, 2], dielectrics [2–5], polymers [6] and metals [7–9]. The problem has also been broadly addressed in the recent literature [10]. However, most of the optically transparent materials, which have attracted attention due to their various applications, are resistant to intense long-wavelength radiation. For example, polymers and dielectrics exhibit very low linear absorption coefficient values in the near-infrared (NIR) spectral region. Hence the laser ablation threshold is very high for these materials [6], which results in a low machining efficiency [3].

In a recent work [11], we have demonstrated a new method in which visible (vis) and extreme ultraviolet (XUV) beams are combined to modify the surface of an otherwise infrared (IR)-transparent poly(methyl methacrylate) (PMMA) sample. This method addresses the problem of the efficiency of structuring the surface of IR-radiation-resistant materials. In this paper, we present new results showing that the method is also applicable for the more efficient creation of rippled or laser-induced periodic surface structures (LIPSS); nanostructures on amorphous carbon (a-C) provide a tool for quickly modifying the tribological properties of the sample. We also discuss how LIPSS structures arise when the *dual-action* technique is used.

2. Experimental setup

In the demonstration of our method [11], we investigated PMMA and showed that if femtosecond NIR laser pulses generated by a titanium–sapphire laser system are applied simultaneously with an XUV beam, the surface processing efficiency is significantly enhanced when compared with the case when NIR pulses alone are applied. Both uniform material expansion and spikes formation, which are quite unique responses, were observed in these initial experiments.

Here, we present our recent results of the surface nanostructuring of a-C samples using this technique. The experimental setup is shown in figure 1. For highly efficient XUV high-order harmonic generation, a two-colour laser field scheme was developed, built and optimized [12, 13]. Femtosecond laser pulses at the central wavelength of 820 nm with an energy

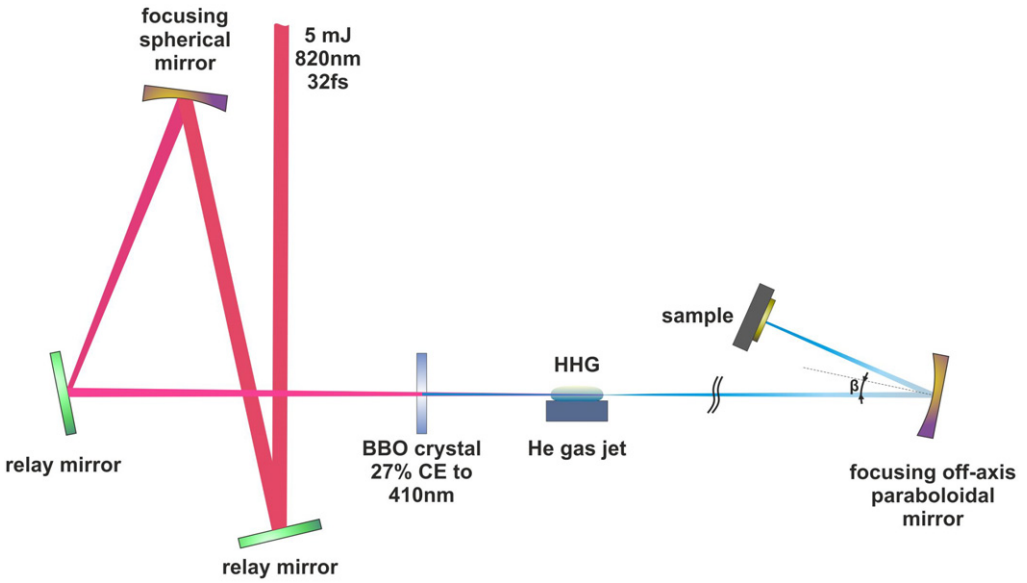

Figure 1. The experimental setup. High-order harmonic generation was obtained in the so-called 'two-colour' scheme. NIR femtosecond laser pulses were focused by a spherical mirror into the longitudinal He gas jet. A BBO crystal was placed between the jet and the mirror to generate SH of the fundamental laser field with a CE of 27%. All the beams (NIR at 820 nm, vis at 410 nm and XUV at 21.6 nm) were focused by an OAP mirror on a sample.

of 5 mJ and pulse duration of 32 fs, 10 Hz were focused using a spherical mirror ($f = 600$ mm) into a He gas jet. For second harmonic (SH) generation a 200 μm-thick β-barium borate (BBO) was placed 400 mm from the focusing mirror providing a conversion efficiency (CE) into SH of about 27%. A gas jet with a slit nozzle of 0.5 mm width and 6 mm length was used. The pressure in the interaction region was $\sim$200 mbar. The XUV source was optimized for the strongest spectral line at 21.6 nm and characterized using a flat-field soft x-ray spectrometer. It provided 150 nJ per pulse at the 38th harmonic order. The remaining NIR–vis and XUV beams were all focused by a multilayer (Mo/Si) off-axis paraboloidal (OAP) mirror ($f = 125$ mm, 13°, $R = 37\%$ at 21 nm). A sample was placed at a fixed distance of 125 mm from the OAP. In the case where the sample was irradiated solely by NIR–vis radiation, the gas puff was turned off. Since the CE into XUV radiation of the setup was $\sim 10^{-5}$, we consider the NIR–vis beam intensity as not yet depleted if harmonics are generated and illuminate the sample together with NIR–vis beams. We did not observe any changes in the transverse mode profile of the NIR–vis beams when the gas puff was turned on or off.

We have examined two types of samples: a 500 nm layer of PMMA spin coated on a 315 μm-thick silicon substrate (Silson, UK) and an 890 nm layer of a-C deposited by magnetron sputtering on a bulk silicon substrate (GKSS Research Centre, Germany). The morphology of the irradiated target surfaces was investigated with a Nomarski differential interference contrast microscope (BX50M and BX60M) and with an atomic force microscope (AFM; Dimension 3100 driven by a NanoScope IV controller; Veeco, USA) operated in the tapping mode. The estimated single-shot average fluences on the sample surface were 45 mJ cm^{-2} at 820 nm, 18 mJ cm^{-2} at 410 nm and 0.3 mJ cm^{-2} at 21.6 nm. All these values lie far below the ablation

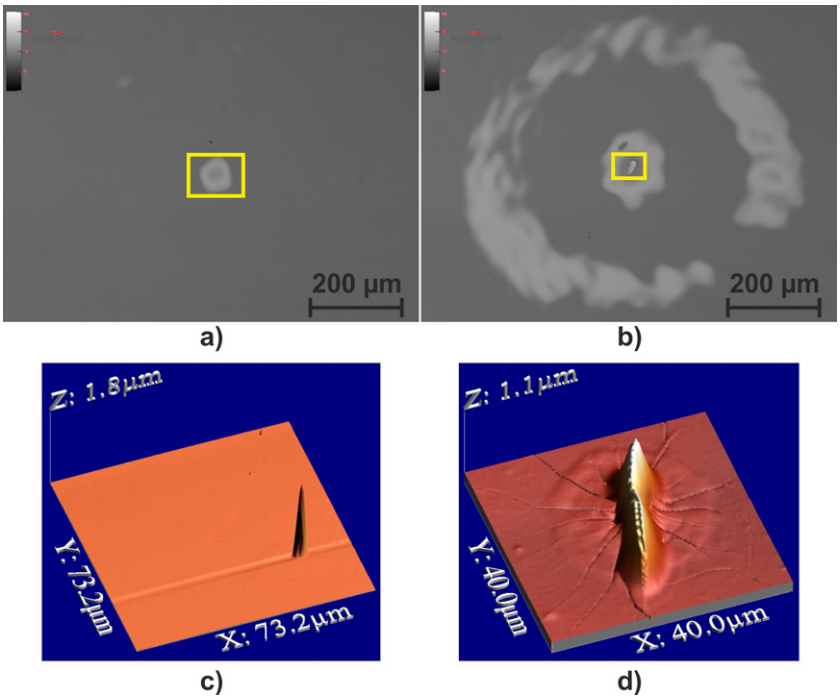

Figure 2. Experimental results of PMMA exposure. Images from a Nomarski microscope of PMMA samples exposed to (a) a single shot of ∼63 mJ cm^{-2} of NIR–vis radiation alone and (b) a mixed field of XUV/NIR–vis (45 mJ cm^{-2} at 820 nm, 18 mJ cm^{-2} at 410 nm and 0.3 mJ cm^{-2} at 21.6 nm). The corresponding AFM images of the details in (a) and (b) are presented in (c) and (d), respectively. The ring visible in (b) is a result of diffraction at the aperture defining the NIR beam size.

threshold for PMMA in the NIR (2.6 J cm^{-2} for a single shot and 0.6 J cm^{-2} for 100 shots [14]) as well as in the XUV (2 mJ cm^{-2} [15]) spectral regions. The contribution of other harmonic orders is negligible due to the high spectral selectivity of the multilayer structure of the OAP mirror (in the EUV range centred at 21.6 nm). There are very few data on the ablation threshold of a-C. For multi-pulse irradiation of polycrystalline carbon by 100 fs laser pulses at 800 nm, the ablation threshold is estimated to be of the order of a few J cm^{-2} [16]. For 25 fs, free-electron laser pulses at 32.5 nm and a-C layer thickness of 46 nm, the single-shot ablation threshold is ∼60 mJ cm^{-2} (estimation error ∼50%) [17]. For a 1.7 ns, Ne-like Ar capillary discharge laser at 46.9 nm, the ablation threshold has been estimated to be ∼1.1 J cm^{-2} in the single-pulse irradiation regime [18]. The irradiation conditions did not change for the two samples.

3. Results

Figure 2 shows the experimental results of PMMA processing. Figure 2(a) presents an image from a Nomarski DIC microscope of the sample irradiated with NIR–vis photons alone (∼63 mJ cm^{-2} in total), whereas figure 2(b) shows the sample exposed to the combined XUV/NIR–vis field (45 mJ cm^{-2} at 820 nm, 18 mJ cm^{-2} at 410 nm and 0.3 mJ cm^{-2} at 21.6 nm). The sample irradiated solely with NIR–vis light exhibits negligible surface changes, while

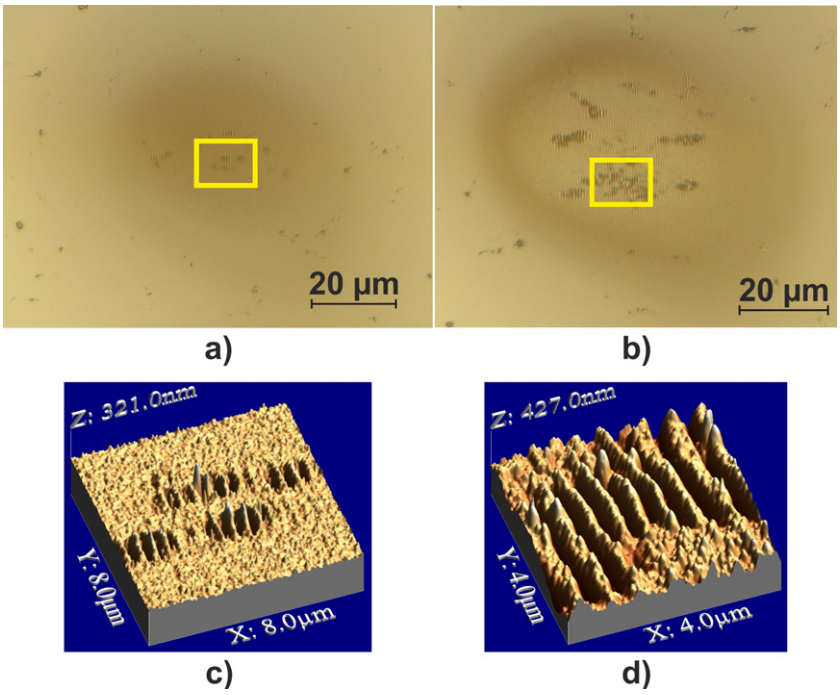

Figure 3. Experimental results of a-C exposure. Nomarski microscope images of a-C samples exposed to 10 shots of (a) an NIR–vis beam alone ($\sim$63 mJ cm^{-2}) and (b) XUV/NIR–vis (45 mJ cm^{-2} at 820 nm, 18 mJ cm^{-2} at 410 nm and 0.3 mJ cm^{-2} at 21.6 nm). The corresponding AFM scans of the details are presented in (c) and (d).

in the case of combined fields the area of the modified surface dramatically increases and material expansion is observed. Figures 2(c) and (d) show AFM scans of the surface changes in the vicinity of the beam centre (marked with rectangles) of panels (a) and (b), respectively. The experiment was performed in the single-shot regime. The root mean square (rms) microroughness of the samples illuminated by NIR–vis and XUV/NIR–vis was estimated to be 4.7 and 176.5 nm, respectively (evaluated only in the interaction region), while that of the unexposed sample was 5.7 nm [19].

Even stronger enhancement of the surface processing by the dual action was observed on the a-C sample (figure 3). LIPSS, or 'ripples', with a spatial period of $\sim$550 nm were created during 10-shot exposure in both cases; however, a clear difference was observed in modulation depth: the peak-to-valley depth was $\sim$130 nm for the NIR–vis ($\sim$63 mJ cm^{-2})-irradiated sample (figures 3(a) and (c)), whereas it was $\sim$200 nm for the combined XUV/NIR–vis fields (45 mJ cm^{-2} at 820 nm, 18 mJ cm^{-2} at 410 nm, and 0.3 mJ cm^{-2} at 21.6 nm; figures 3(b) and (d)). Moreover, despite its random distribution, the frequency of occurrence of LIPSS is much higher in the case of the dual-field irradiation. A detailed analysis of AFM scans revealed that in the case of figure 3(a), only about 4% of the interaction region was covered with LIPSS, whereas in the case of figure 3(b) it was as much as 27%. In the case of the samples shown in figure 3, the rms microroughness was 13.5 nm for NIR–vis irradiation, 46.2 nm for XUV/NIR–vis and 8.3 nm for the unexposed sample. A detailed view of LIPSS created on a-C by dual action is presented in figure 4. The general view of these structures is presented in figure 7.

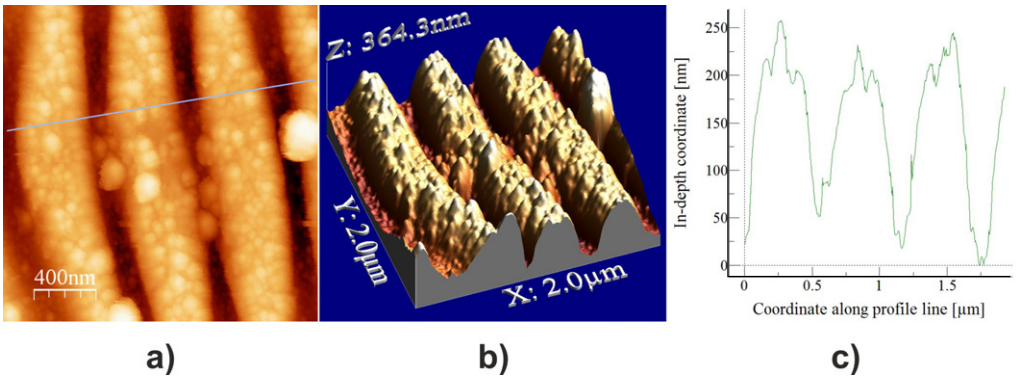

Figure 4. Characteristics of LIPSS obtained by 'dual action' on the surface of a-C. A very specific curved shape of LIPSS was observed (a), which was clearly visible also in the 3D visualization (b). The profile (c) along the grey line in (a) provides the characteristic dimensions of the obtained structures. Irradiation conditions were the same as those in figure 3.

The efficiency of the dual action is much higher than that in our previous experiment [11] owing to the larger output from the driving Ti-doped sapphire laser system. Here, using only a single shot, we obtained structures (figure 2(d)) similar to those achieved with 50 shots earlier.

4. Laser-induced periodic surface structures creation mechanism

Since the first observation of them in 1965 [20], the formation of LIPSS has been frequently reported in the literature. Typically, LIPSS are observed in many different samples: dielectrics, metals and semiconductors. In general, two distinct types of LIPSS structures are known: (i) LIPSS-I (also referred to as LIPSS of the first kind, or coherent LIPSS) and (ii) LIPSS-II (also known as LIPSS of the second kind, or incoherent LIPSS) [21]. LIPSS-I display dependences on wavelength, polarization, coherence properties and angle of incidence of the laser beam. They are usually observed at the outer side of the interaction crater where the fluence does not exceed the ablation threshold [22]. In contrast to LIPSS-I, incoherent LIPSS are sensitive to total energy deposition on the sample and the laser pulse duration. They appear in the centre of the crater. A majority of the initial experiments on the creation of LIPSS were performed using continuous wave, nanosecond or sub-nanosecond laser pulses. Later, LIPSS were also produced by using laser systems providing pulses of ultrashort duration of the order of fs) [23]. In most recent experiments, laser pulses with duration >100 fs were used. Usually, the fluence is adjusted to fall just below the ablation threshold of an investigated material, and typically 20–30 NIR laser pulses are needed to obtain ripple structures on surfaces. The entire range of currently available laser sources allows the study of different LIPSS to show their dependence on the laser pulse duration, light coherence, polarization, fluence on the sample, total dose of deposited radiation, etc.

Even though nearly 50 years have passed since the publication of Birnbaum's work [20], the LIPSS mechanism remains ambiguous. Initially LIPSS-I were interpreted using a simple model where the interference between the incident light and waves scattered at material inhomogeneities induced the creation of periodic surface structures [22]. The scattered wave

was assumed to propagate along the target surface. The first LIPSS model described in detail in [24], however, did not explain, for example, the relationship between LIPSS period and the value of the index of refraction of the sample. The problem was addressed by using a more sophisticated *radiation remnants* model [25]. In general, there are two conditions to be fulfilled for successful LIPSS creation. One is the aforementioned interference. The other is the response of the sample material to the periodic modulation of deposited energy. In most cases the first model is used. When a more sophisticated approach is needed to match the experimental results, the second one is used.

Previous works have pointed out interesting LIPSS properties. Of particular interest is [26]. The authors of [26] show that SEM images reveal that crests of LIPSS-I structures created on a krypton-doped silicon sample are strongly affected by krypton bubbles which emerge from the sample material through the silicon surface. This clearly indicates that at these sites the melting process took place. Other publications explain LIPSS-II by means of 'frozen' acoustic [27, 28] or capillary [28] waves, as well as by thermocapillary [29] or Kelvin–Helmholtz [30] instabilities.

The physical mechanism of LIPSS formation like that observed in our experiments has been broadly discussed in the literature [1–9], [14]. A few of the phenomena present when LIPSS are created using femtosecond laser pulses have been suggested (such as the incubation effect, free charge carrier absorption preceded by ionization of the surface of a material, neutral atom desorption and positive ion emission due to Coulomb explosion); however, the complete process has not been elucidated yet. Thus, based on known physical mechanisms and our observation a new, broader scenario is proposed to explain LIPSS creation using IR/vis together with XUV ultrashort pulses.

We have observed that the XUV–NIR dual action significantly increases the efficiency of material surface structuring and LIPSS production. To explain this enhancement, we refer to the observation of the creation of LIPSS structures of the second kind. In order to obtain these structures there had to take place very strong isochoric heating of the near-surface volume by impinging a laser pulse. Such a temperature increase leads to the rapid growth of pressure in the interaction region. This very unstable state relaxes through material melting and formation of rippled structures that make possible a reduction in local tensions on the material surface. The NIR radiation is strongly absorbed thanks to the creation of defects (e.g. colour centres) in the material, which is normally transparent in this spectral range [31, 32]. It has been shown that it is possible to create defects with the use of UV and XUV photons [33] as well as with ultra-intense NIR laser radiation, which are responsible for the *incubation effect* [34]. The creation of colour centres results in the appearance of new electronic states inside the material band gap, leading to enhancement of absorption through these states [5]. In our case, the presence of such defects is inferred from figure 2(a), where material modification can be clearly seen with the Nomarski optical microscope but, surprisingly, no surface modification at all is found in the corresponding AFM images (cf the inset of figure 2(a)). Nevertheless, it should be stressed that the development of defects takes a much longer time than the duration of the laser pulses used in our experiment (32 fs). Thus absorption through new energy levels located in the bandgap, having their origin in the appearance of defects, is not expected to play a key role in our experiment. The strong coupling of the NIR laser beam with XUV/NIR-irradiated solids might then be attributed to efficient creation of free electrons through linear absorption of highly energetic XUV photons. The occurrence of free electrons during the LIPSS creation process has been proved using time-of-flight mass spectrometer measurements [35]. The clouds

of free electrons are subsequently subjected to free-carrier absorption of NIR light, leading to an increase in the absorption coefficient of optical radiation.

It has been proven by ultrafast electron diffraction measurements that before the rippled structures are created, a very thin layer of material (∼30–40 nm) on the surface of the sample is melted as a consequence of a non-thermal phase transition induced by very intense femtosecond laser pulses [36].

In order to verify whether phase transition took place in our experiment, we performed Raman measurements, in the usual back scattering geometry, with a Raman spectrometer (Renishaw Ramascope; UK) equipped with a CCD camera and a Leica DMLP microscope. Typically, Ar^+ laser (514.5 nm) spots with a diameter of 4 μm were used. This tool enabled us to probe selected locations on the sample surface.

Typical Raman spectra of a-C exhibit, at 1530 cm^{-1}, the shape of two overlapping bands: a high-frequency G-band and a low-frequency D-band. An increase in D-band is indicative of graphitic sheets growing in the material; for details, see, for example, [37]. In figure 6, a remarkable increase in D-band can be seen in both areas damaged by long-wavelength radiation (figure 6(a)) as well as by the mixed field of long- and short-wavelength radiation (figure 6(b)). Thus the presence of a high degree of graphitization in the a-C layer exposed to multiple shots of NIR–vis and XUV/NIR–vis radiation was proved.

When a material surface is molten, convective mass transport can be considered. The material is subjected to spatial modulation of light intensity originating from the interference of the light scattered on inhomogeneities (inclusions or defects) in the material with the incident beam (as assumed by LIPSS theory). The sites of higher enthalpy correspond to the crest of the intensity distribution waveform. In other words, there is spatial modulation of pressure in the molten material. At places where the pressure is higher, there is a temporary force exerted on each liquid particle, and the magnitude of the force vector will be proportional to the local pressure. Globally, there will be modulation of the pressure gradient with direction towards the sites where the pressure is highest (or, equivalently, the intensity is highest). In such a 'liquid', collective behaviour in the form of convection currents is expected (analogous to the well-known phenomenon of convective currents induced by Gaussian laser beams) [38, 39]. Such convective currents cause the transport of the material into areas of higher-light-intensity sites (figure 5). To confirm our hypothesis, we have performed simulations of the intensity pattern created on the surface of material by the interference of light scattered on the surface (e.g. on F-centres) and the incident beam. The structure of the periodic surface pattern shown in figures 4(a) and (b) and figure 7(a) is predominantly determined by a transverse periodic intensity distribution as, for example, depicted in figure 7(b). Such modulation of the intensity is usually attributed to two or more mutually interfering light waves. In the following, the interference between the incident field and the back-reflected field from a spherical grain in the material is considered as a model (just as in [24]).

As the input parameters of the model, we insert complex indices of refraction of both the spherical grain ($n_1 = 2.5–0.8i$; assumed value) and surrounding material ($n_2 = 2.624–0.657i$; measured experimentally using the samples of a-C engaged in the experiment), the radius of the sphere ($R = 50$ nm), distance of its centre to the observation plane ($d = 300$ nm) and initial polarization vector (parallel to the Y-axis in figure 7(b)). Let us assume a planar linearly polarized wave travelling through a pristine material having a complex index of refraction. Such a wave can propagate freely unless it hits an impurity lying beneath the sample surface and reflects back towards the tail of the impinging pulse. The wave, reflected from a spherical

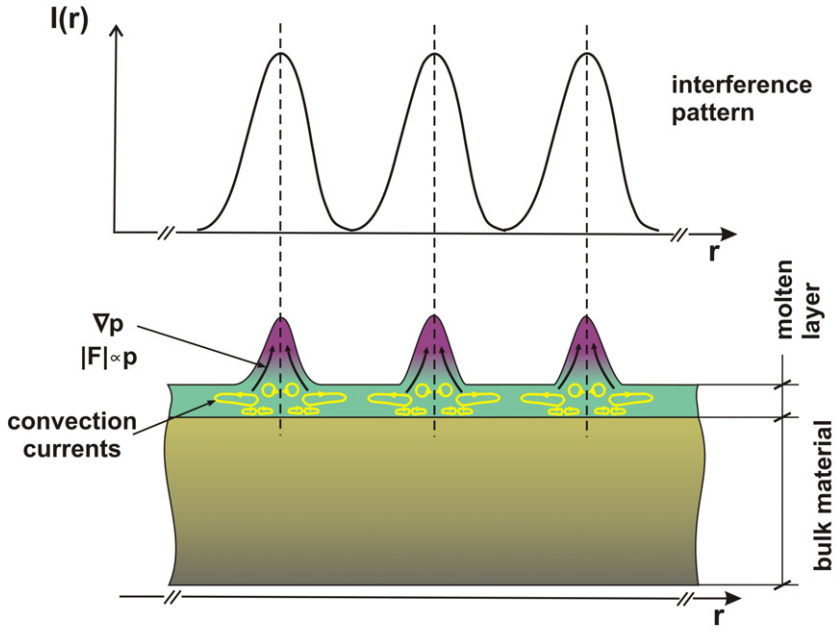

Figure 5. Convection current model. A thin layer of the bulk material is molten (thickness of the order of tens of nm) after irradiation by a femtosecond NIR laser. During NIR pulse radiation, when the molten material is subjected to the interference pattern (upper part of the figure), a spatial modulation of the pressure will be established, leading to the creation of local pressure gradients. In the areas where the pressure is higher, the 'hotter' liquid will expand by means of convection currents (along the pressure gradient).

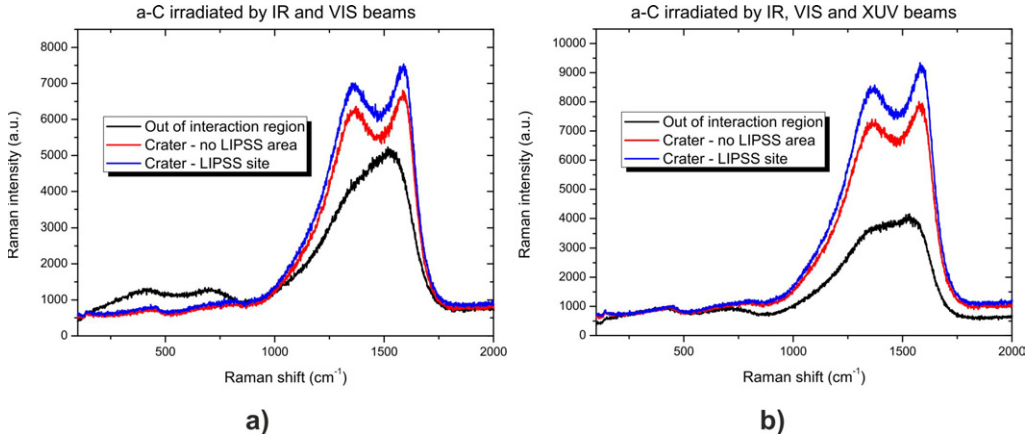

Figure 6. Raman spectra of a-C samples irradiated by IR and vis femtosecond laser pulses (a) and by IR/vis together with XUV beams.

surface, has to be treated numerically for all points of the sphere. At each point of the half-sphere the reflectivity for the transverse electric (TE) and transverse magnetic (TM) compounds of the electrical vector is determined from the Fresnel equations. The reflectivity of the TE wave increases to unity with angle of incidence, whereas the reflectivity of the TM wave first reaches

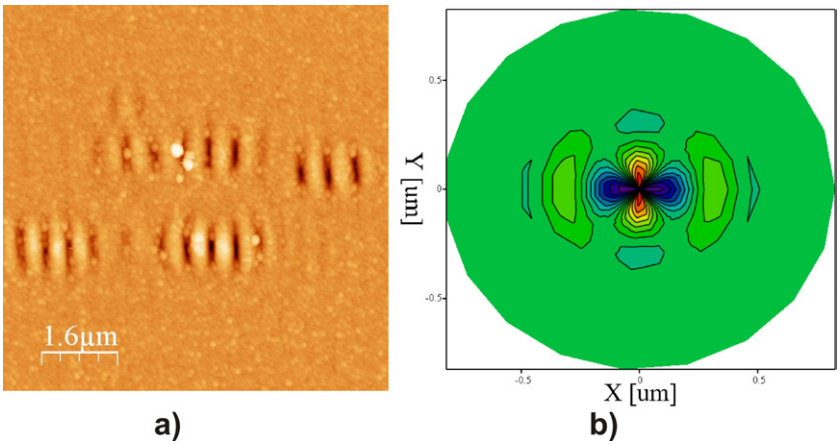

Figure 7. Comparison of the experimental and the simulated LIPSS. The observed shape of LIPSS (a) exactly mimics the simulated interference pattern (b), figures 4(a) and (b). The lowest intensity values in (b) correspond to blue colour in the picture, while red colour corresponds to the highest intensity sites. The polarization vector orientation was vertical.

its minimum at Brewster's angle and then rises to unity (total reflection). This, in fact, introduces anisotropy into the reflected field. Furthermore, the TM compound of the polarization vector, which was originally parallel to the sample surface, changes its direction with respect to the direction of the back-reflected ray. As a consequence of both effects, the interference pattern in the observation plane above the sphere has a form of linear fringes parallel to the initial polarization vector as illustrated in figure 7(a) and (b). Finally, it is important to stress that the above-described model was developed solely to elucidate the structure of the observed surface pattern. For the purposes of a more detailed analysis, Mie scattering is to be incorporated into the simulation, which is, however, beyond the scope of this paper.

A comparison shows that the shape of the simulated pattern (figure 7(b)) unambiguously mimics the curved shape of the LIPSS structures visible in figure 7(a), as well as in figure 4(a) and in figure 4(b), showing a direct correlation between the shape of the light interference pattern and the shape of generated LIPSS. We did not observe any difference in shape between LIPSS created by NIR–vis beams and those created by the combined XUV/NIR–vis field. Hence, scattering is attributed exclusively to NIR–vis beams.

5. Conclusion

In conclusion, we have experimentally demonstrated that the dual action of NIR–vis and XUV femtosecond pulses affects materials differently, i.e. molecular PMMA and covalent a-C solids. The dual action achieves enhanced efficiency of surface processing of both materials. XUV radiation-induced formation of defects and free-charge carriers leads to alteration of the NIR–vis optical properties of the processed material. In the case of a-C, large areas of LIPSS with a spatial period of 550 nm are created that have their origin in laser-induced convective currents. Their formation is a proof of the occurrence of melting in the near-surface carbon layer.

Acknowledgments

This research was supported by the Czech Science Foundation (grant number 202/07/J008), by the Czech Ministry of Education (grant numbers LC528, LC510, ME10046 and LA08024), by the Academy of Sciences of the Czech Republic (grant numbers M100100911, KAN300100702 and Z10100523) and by the Ministry of Education, Science and Technology of Korea through the National Research Foundation.

References

[1] Costache F, Kouteva-Arguirova S and Reif J 2004 Sub-damage-threshold femtosecond laser ablation from crystalline Si: surface nanostructures and phase transformation *Appl. Phys.* A **79** 1429–32
[2] Varlamova O, Costache F, Reif J and Bestehorn M 2006 Self-organized pattern formation upon femtosecond laser ablation by circularly polarized light *Appl. Surf. Sci.* **252** 4702–6
[3] Krüger J and Kautek W 1996 Femtosecond-pulse visible laser processing of transparent materials *Appl. Surf. Sci.* **96–98** 430–8
[4] Stoian R *et al* 2000 Ion time-of-flight analysis of ultrashort pulsed laser-induced processing of Al_2O_3 *Appl. Surf. Sci.* **165** 44–55
[5] Henyk M, Costache F and Reif J 2002 Ultra short laser pulse ablation from sodium chloride—the role of laser induced color centers *Appl. Surf. Sci.* **197–198** 90–5
[6] Krüger J and Kautek W 2004 Ultrashort pulse laser interaction with dielectrics and polymers. *Adv. Polym. Sci.* **168** 247–89
[7] Sakabe S, Hashida M, Tokita S, Namba S and Okamuro K 2009 Mechanism for self-formation of periodic grating structures on a metal surface by a femtosecond laser pulse *Phys. Rev. B* **79** 033409
[8] Tsukamoto M *et al* 2006 Periodic microstructures produced by femtosecond laser irradiation on titanium plate *Vacuum* **80** 1346–50
[9] Yasumaru N, Miyazaki K and Kiuchi J 2005 Fluence dependence of femtosecond-laser-induced nanostructure formed on TiN and CrN *Appl. Phys.* A **81** 933–7
[10] Gattass R R and Mazur E 2008 Femtosecond laser micromachining in transparent materials *Nat. Photonics* **2** 219–25
[11] Mocek T *et al* 2009 Surface modification of organic polymer by dual action of extreme ultraviolet/visible-near infrared ultrashort laser pulses *J. Appl. Phys.* **105** 026105
[12] Kim I J *et al* 2005 Highly efficient high-harmonic generation in an orthogonally polarized two-color laser field *Phys. Rev. Lett.* **94** 243901
[13] Kim I J *et al* 2008 Generation of submicrojoule high harmonics using a long gas jet in a two-color laser field *Appl. Phys. Lett.* **92** 021125.
[14] Baudach S, Bonse J, Krüger J and Kautek W 2000 Ultashort pulse laser ablation of polycarbonate and polymethylmethacrylate *Appl. Surf. Sci.* **154–155** 555–60
[15] Chalupsky J *et al* 2007 Characteristics of focused soft x-ray free-electron laser beam determined by ablation of organic molecular solids *Opt. Express* **15** 6036
[16] Kononenko V V *et al* 2005 Effect of the pulse duration on graphitisation of diamond during laser ablation *Quantum Electron.* **35** 252–6
[17] Hau-Riege S P *et al* 2007 Damage threshold of inorganic solids under free-electron-laser irradiation at 32.5 nm wavelength *Appl. Phys. Lett.* **90** 173128
[18] Juha L *et al* 2009 Radiation damage to amorphous carbon thin films irradiated by multiple 46.9 laser shots below the single-shot ablation threshold *J. Appl. Phys.* **105** 093117
[19] Horcas I *et al* 2007 WSXML: a software for scanning probe microscopy and a tool for nanotechnology *Rev. Sci. Instrum.* **78** 013705
[20] Birnbaum M 1965 Semiconductor surface damage produced by ruby lasers *J. Appl. Phys.* **36** 6988

[21] Bäuerle D 1996 *Laser Processing and Chemistry* (Berlin: Springer)
[22] Emmony D C, Howson R P and Willis L J 1973 Laser mirror damage in germanium at 10.6 μm *Appl. Phys. Lett.* **23** 598
[23] Wu Q *et al* 2003 Femtosecond laser-induced periodic surface structure on diamond film *Appl. Phys. Lett.* **82** 1703–5.
[24] Guosheng Z, Fauchet P M and Siegman A E 1982 Growth of spontaneous periodic surface structures on solids during laser illumination *Phys. Rev.* B **26** 5366
[25] Sipe J E, Young J F, Preston J S and van Driel H M 1983 Laser-induced periodic surface structure. I. Theory *Appl. Phys.* B **28** 1141
[26] Oron M and Sorensen G 1979 New experimental evidence of the periodic surface structure in laser annealing *Appl. Phys. Lett.* **32** 782
[27] Jost D *et al* 1986 Laser pulse width dependent surface ripples on silicon *Appl. Phys. Lett.* **49** 625
[28] Gorodetsky G *et al* 1985 Far UV pulsed laser melting of silicon *Appl. Phys. Lett.* **46** 547
[29] Shen M Y *et al* 2003 Formation of regular arrays of silicon microspikes by femtosecond laser irradiation through a mask *Appl. Phys. Lett.* **82** 1715
[30] Ang L K *et al* 1998 Surface instability of multipulse laser ablation on a metallic target *J. Appl. Phys.* **83** 4466
[31] Hayes W and Stoneham A M 1985 *Defect and Defect Processes in Nonmetallic Solids* (New York: Wiley)
[32] Schulman J H and Compton W D 1962 *Color Centers in Solids* (Oxford: Pergamon)
[33] Kudryavtseva I *et al* 2001 Color center formation by synchrotron radiation in the $Na_6Al_6Si_6O_{24}(Nal)_{1.6}$ optical ceramic *Phys. Solid State* **43** 5
[34] Reif J 1989 High power laser interaction with the surface of wide bandgap materials *Opt. Eng.* **28** 1122–32
[35] Henyk M, Mitzner R, Wolfframm D and Reif J 2000 Laser-induced ion emission from dielectrics *Appl. Surf. Sci.* **154–155** 249–55
[36] Siwick B J, Dwyer J R, Jordan R E and Miller R J D 2003 An atomic level view of melting using femtosecond electron diffraction *Science* **302** 1382–5
[37] Ferrari A C and Robertson J 2000 Interpretation of Raman spectra of disordered and amorphous carbon *Phys. Rev.* B **61** 14095
[38] Hao L and Lawrance J 2005 *Laser Surface Treatment of Bio-Implant Materials* (New York: Wiley)
[39] Ravindran K, Srinivasan J and Marathe A G 2004 Finite-element study of the role of convection in laser-surface melting *Numer. Heat Transfer* A **26** 601–18